Chemical Systems Biology Reveals Mechanisms of Dissociated Glucocorticoid Receptor Signaling

Nelson E. Bruno[1], Jerome C. Nwachukwu[1], Sathish Srinivasan[1], Charles C. Nettles[1], Tina Izard[1], Zhuang Jin[2*], Siddaraju V. Boregowda [2], Donald G. Phinney[2], Olivier Elemento[3], Xu Liu[4], Eric A. Ortlund[4], René Houtman[5], Diana A. Stavreva[6], Gordon L. Hager[6] , Theodore M. Kamenecka[2], Douglas J. Kojetin[1,2], Kendall W. Nettles[1].

1. Department of Integrative Structural and Computational Biology, The Scripps Research Institute, Jupiter, FL 33458 USA
2. Department of Molecular Medicine, The Scripps Research Institute, Jupiter, FL 33458 USA
3. Caryl and Israel Englander Institute for Precision Medicine, Institute for Computational Biomedicine, Department of Physiology and Biophysics, Weill Cornell Medicine, New York, NY 10065, USA
4. Department of Biochemistry, Emory University School of Medicine, Atlanta, GA 30322, USA
5. Department of Research and Development, PamGene, 's-Hertogenbosch, 5211 HH, the Netherlands.
6. Laboratory of Receptor Biology and Gene Expression, Building 41, B602, 41 Library Dr., National Cancer Institute, NIH, Bethesda, MD 20892-5055, USA

* Current affiliation: Corbus Pharmaceuticals, Inc. 500 River Ridge Dr. Norwood, MA 02062.

Correspondence: Kendall Nettles, knettles@scripps.edu

Abstract

Glucocorticoids display remarkable anti-inflammatory activity, but their use is limited by on-target adverse effects including insulin resistance and skeletal muscle atrophy. We used a chemical systems biology approach Ligand Class Analysis (LCA) to examine ligands designed to modulate glucocorticoid receptor activity through distinct structural mechanisms. These ligands displayed diverse activity profiles, providing the variance required to identify target genes and coregulator interactions that were highly predictive of their effects on myocyte glucose disposal and protein balance. Their anti-inflammatory effects were linked to glucose disposal but not muscle atrophy. This approach also predicted dissociated activity *in vivo*, identifying compounds that were muscle sparing or anabolic for protein balance and mitochondrial potential. LCA defines the mechanistic links between the ligand-receptor interface and the ligand-driven physiological outcomes, a general approach that can be applied to any ligand-regulated allosteric signaling system.

Introduction

Glucocorticoids (GCs) are among the most prescribed medicines due to their remarkable anti-inflammatory effects. GCs also cause insulin resistance, reduce glucose uptake in skeletal muscle—the organ responsible for ~80% of glucose disposal—and facilitate muscle wasting by reducing protein synthesis and increasing protein degradation[1,2]. Efforts to develop improved GCs have been hampered by poor understanding of the structural and molecular mechanisms through which glucocorticoid receptor (GR) ligands drive diverse phenotypic outcomes, such as effects on inflammation, glucose disposal, or skeletal muscle atrophy. This phenomenon is called selective modulation or dissociated signaling, and is a common feature of allosteric signaling through GR and other nuclear receptor superfamily transcription factors[3], G protein-coupled receptors, and other small molecule drug targets.

GCs are secreted by the adrenal gland in a circadian fashion and in acute response to nutrient deprivation or other stressors. In skeletal muscle, GCs stimulate catabolic signaling that opposes the insulin/PI3K/AKT signaling pathway, inhibits glucose uptake, and releases amino acids by inhibiting protein synthesis and stimulating protein degradation[2]. Upon GC binding, GR dissociates from inhibitory heat shock protein complexes and translocated to the nucleus, oligomerizes upon binding to DNA, and recruits an ensemble of coregulators, which include chromatin-remodeling and histone-modifying enzymes that regulate gene expression. Several GR coregulators and target genes have been identified in skeletal muscle[4-7], but factors that drive ligand-selective modulation are unclear.

We developed a chemical systems biology approach called Ligand Class Analysis (LCA) to identify molecular mechanisms that drive ligand-selective signaling[8-10]. With LCA, we characterize a series of related compounds that display a full range of variance in phenotypes such

62 as insulin-mediated glucose uptake or protein synthesis and use that variance to identify molecular
63 predictors of the phenotype. This enables us to identify ligand-dependent gene expression and
64 protein-interaction profiles that predict molecular phenotypes induced by different classes of
65 ligands that perturb receptor structure differently[8-10]. We then overexpress or knockdown
66 predictive genes or interacting proteins to determine which factors are required for ligand-
67 dependent phenotypes.

68 In this work, we evaluated the physiological effects of GCs during overnight nutrient
69 deprivation when they coordinate acute metabolic adaptations, including effects on glucose
70 disposal and protein balance. We tested a series of GCs modified at different positions on the
71 steroidal scaffold[11], providing distinct strategies to perturb GR structure and dynamics. Using a
72 machine learning approach with LCA, we found that the effects of GCs on protein balance in
73 skeletal muscle can be dissociated from their effects on glucose disposal and the inflammatory
74 response, allowing us to discover the underlying coregulators and genes driving these activities,
75 and discover orally available dissociated glucocorticoids with muscle-sparing activity profiles in
76 vivo.

77

78 **Results**

79

80 **Development of a physiologically relevant skeletal muscle profiling platform for effects of**
81 **GCs on glucose disposal and protein balance during nutrient deprivation**

82 We designed a series of GCs to test the role of three different structural perturbations found in
83 compound PF-0251802 (PF802) (**1**, **Figure 1a**)[12], a dissociated GR ligand, the pro-drug of which
84 reached clinical trials [13]. PF802 has a benzyl group to drive antagonism by disrupting the agonist-

85 bound GR conformation (**Figure 1b**), similar to the carbon-11 (C11) substitution in the antagonist
86 RU-486 (**Figure 1c**), and a trifluoromethyl group attached at the equivalent position of C17 on a
87 steroid to increase affinity (**Figure 1c-d**). PF802 also contains a methylpyridinyl acetamide group
88 attached at the equivalent position to C3 in the steroid scaffold. We predict that this group enters
89 the solvent channel underneath the coregulator binding site, as first seen with deacylcortivazol
90 (**Figure 1e**), to alter the shape of AF2, and the ensemble of coregulators that bind this surface, thus
91 driving dissociated effects as we previously showed for the estrogen receptor[9,14].

92 To understand the how these different substitutions control GR activity, we generated a set
93 of 22 related compounds based on a steroidal core, which enabled us to understand where
94 substitutions are directed within the ligand-binding site (**6-27**, **Figure 1f-g**). These included a
95 number of substitutions at C11 to drive agonism/antagonism (**13-20 Figure 1g**), different
96 substitutions at C17 to optimize affinity (**21-24**, **Figure 1g**), and the methylpyridinyl acetamide at
97 C3 to perturb the AF2 surface (**6-12**, **Figure 1g**), where the position of methyl and nitrogen in the
98 pyridine ring were altered. We have published the synthesis and preliminary structure-activity
99 relationships for these compounds[11].

100 We developed a profiling platform to examine how ligand-regulated GR nuclear
101 localization, structure, and target gene expression in skeletal muscle control glucose disposal and
102 protein balance (**Figure 1h, Methods**), and whether these effects could be dissociated from anti-
103 inflammatory effects such as the suppression of IL-6 secretion by A549 lung cells. We assayed
104 ligand-induced nuclear translocation of a GFP-GR fusion protein, and probed for ligand-selective
105 changes in surface structure by characterizing the GR-interaction profiles of 154 peptides derived
106 from nuclear receptor coregulators and other interacting proteins using the MARCoNI FRET
107 assay[15]. We also completed nascent RNA expression profiling of C2C12 myotubes, one hour after

108 vehicle or Dexamethasone (Dex) treatment and selected 28 target genes as potential regulators of
109 glucose disposal and protein balance (the rationale for compound selection is in **Supplementary**
110 **Information Methods**). We then compared ligand-dependent regulation of these target genes in
111 myotubes using the nanoString nCounter for direct multiplexed transcript counting without PCR
112 amplification**,** enabling highly quantitative and reproducible assays[16]. These datasets comprise the
113 independent variables that we used in a machine learning approach described below, to identify
114 ligand-selective regulators of glucose disposal and protein balance in skeletal muscle, the
115 dependent variables.

116 To assay physiologically relevant effects of GCs on skeletal muscle, we treated the
117 myotubes in the context of nutrient deprivation and a brief insulin challenge. One of the barriers
118 to understanding GC action in skeletal muscle is that effects on protein balance appear to require
119 50–100 μM Dex *in vitro* [17], despite a ~5 nM Kd for GR. The physiological effects of GCs on
120 protein balance and Glut4 translocation vary *in vivo*, depending upon the stressor. For example,
121 GCs are secreted in response to fasting or exercise, but these stressors have very different effects
122 on skeletal muscle. GCs rapidly induce skeletal muscle atrophy and insulin resistance during
123 fasting, while exercise has opposite effects[18,19]. We found that serum starving the myotubes
124 overnight and administering a brief insulin challenge was sufficient to generate assays with robust
125 signal to noise, suggesting that effects of GR are indeed through inhibiting the insulin/PI3K/AKT
126 signaling pathway[20]. These optimizations enabled highly robust and reproducible assays for
127 glucose disposal and protein balance (see **Methods**), with maximal effects of Dex in the 1-10 nM
128 range (**Supplementary Figure 1a–g**).

129 We developed a screening assay for phosphorylation of AKT at Thr308 (pAKT), reflecting
130 its joint role in coordinating both protein synthesis and glucose disposal (**Supplementary Figure**

131 **1a–b**). For glucose disposal, we measured the rate limiting step, transfer of the glucose receptor,
132 Glut4, to the cell membrane (**Supplementary Figure 1c**). For protein balance, we developed two
133 assays: protein degradation was assayed by release of tritiated phenylalanine (degradation)
134 (**Supplementary Figure 1d**); and insulin-stimulated protein synthesis (synthesis) was assayed
135 using the SUnSET assay (**Supplementary Figure 1e**), which measures the incorporation of
136 puromycin into nascent polypeptide chains. We assessed the relationship between protein balance
137 and mitochondrial potential (ψm) measured by high content imaging after staining with a
138 MitoTracker dye, where accumulation of the dye is dependent upon membrane potential.
139 (**Supplementary Figure 1f–h**). We also compared ligand-dependent effects on IL-1β-induced
140 secretion of IL-6 by A549 lung cells, a standard assay for the inflammatory response. Ligand
141 activity in these assays represent the dependent variables to identify predictive coregulator
142 interactions and target genes, and below, individual compounds with interesting pharmacological
143 properties.

144 After profiling the compounds, we asked which dependent variables show similar ligand
145 response patterns, and identified two clusters, connected by pAKT. In the first cluster, effects of
146 the ligands on protein synthesis were similar to effects on protein degradation, pAKT, and ψm,
147 suggesting transcriptional control via a common set of coregulators and target genes (**Figure 1i,**
148 **Supplementary Figure 1i, Supplementary Dataset** shows the correlation matrix). In the second
149 cluster, effects of the ligands on pAKT showed patterns similar to effects on IL-6 and Glut4
150 (**Figure 1i**), while effects on nuclear translocation of GR also correlated with their effects on IL-6
151 and Glut4. However, effects on pAKT and GR nuclear translocation were dissociated
152 (**Supplementary Figure 1j**). This result indicates that some ligand-dependent outcomes of GR
153 signaling (e.g. Glut4, IL-6) involve a graded response to the amount of nuclear GR, while others

154 require a threshold amount of nuclear GR. Nevertheless, these results suggest that the ligands can
155 use different transcriptional signaling pathways—coregulators and target genes—that coordinate
156 some processes but allow others to be dissociated.
157
158 **Machine learning defines the best sets of predictors for GC effects in skeletal muscle**
159 Using Random Forest, a classification and regression tree algorithm [21], we performed predictive
160 modeling of each GR-mediated phenotype or dependent variable (**Figure 1h**), based on all other
161 features including the independent variables (i.e. GR-peptide interactions and -target genes). To
162 set a statistical threshold, we used *Boruta*, a Random Forest-based wrapper algorithm, to identify
163 a set of predictors for each GR-mediated phenotype, by iteratively comparing the importance of
164 each feature in the dataset, to the highest importance observed in a "shadow" dataset obtained by
165 shuffling every variable [22]. In each of 500 iterative decision rounds, a feature is selected as a
166 predictor if it is more important than the most important shadow feature. In contrast, a feature is
167 rejected if it has not been selected after multiple consecutive decision rounds. We subsequently
168 identified a minimal set of predictors, by applying a forward selection-based strategy. Predictors
169 of each GR-mediated phenotype previously identified via *Boruta*, were tested one-by-one, starting
170 with the most important, for their ability to improve the predictive capacity of the model. Predictors
171 that improved the model were retained, while those that worsened the model were removed, until
172 the set of predictors was expended. With this approach we were able to predict between 46.8%
173 (degradation) and 84.3% (Glut4) of the variance in the dependent variables (**Figure 2a,**
174 **Supplementary Dataset**).
175 This analysis revealed which target genes and interacting peptides were selective or
176 common predictors of the effects of GR ligands on skeletal muscle (**Figure 2a–b, Supplementary**

177 **Figure 2a–b**). The selective prediction of Glut4 but not ψm by the *Bcl2l1* gene was especially
178 striking (**Figure 2b**, **Supplementary Figure 2b**). *Bcl2l1* encodes Bcl-xL, a mitochondrial anti-
179 apoptotic BCL-2 family protein that inhibits glucose metabolism and mitochondrial-mediated
180 secretion of insulin by pancreatic β-cells [23], suggesting that it may also contribute to glucose
181 disposal in skeletal muscle.

182 Linear regression showed that a SMRT peptide interaction with GR significantly predicted
183 synthesis, but not Glut4 or the best Glut4-predictive target genes (**Figure 2c**). There was a striking
184 connection between the coregulator peptides that predicted Glut4, showing very low r^2 with the
185 protein balance assays, but very high predictive power for the specific genes that best predicted
186 Glut4 activity (**Figure 2c**). While the MarCoNI peptide set is best viewed as a probe for ligand-
187 regulated effects on surface structure, all of the peptides in **Figure 2c** represent bona fide nuclear
188 receptor interaction motifs. Thus, we can exploit the variance in ligand activity to identify the
189 common and dissociated transcriptional networks underlying GR-mediated phenotypes in skeletal
190 muscle.

191 The variance in the ligand activity profiles also allowed LCA to identify signal in what
192 would typically be considered noise. Both *Bcl2l1* and *Socs2* showed less than two-fold induction,
193 the standard threshold for noise in gene expression data. Much of the gene expression data
194 displayed an inflection point (**Supplementary Figure 2c**). When we removed the data below the
195 inflection point, *Fkbp5, Blc2l1*, *Tsc22d3* still predicted Glut4 translocation (**Supplementary**
196 **Figure 2d**), suggesting that insulin-mediated glucose disposal can be fine-tuned by very small
197 changes in target gene expression. We call these super-resolution analyses, similar to what we
198 have seen with super-resolution X-ray crystallography, where comparing many structures bound
199 to a series of compounds identified ligand-induced perturbations within the noise of an individual

200 crystal structure that drive biological outcomes[8]. Thus, subtle changes in gene expression that
201 would typically be considered noise and disregarded, are sufficient to identify transcriptional
202 networks underlying GR-mediated phenotypes through LCA.

203 We also found that different substitutions on the steroidal scaffold, designed to perturb
204 different GR differently, modulated distinct transcriptional networks. A comparison of ligand-
205 dependent effects on Glut4 revealed a dramatic increase in predictive power by the C11-substituted
206 compounds compared to the whole compound set, while the C3-substituted compounds exhibited
207 a widespread reduction in r^2 (**Figure 2d–e, Supplementary Figure 2e,** compare to **Figure 2b**).
208 This was evident despite their similar variances in the skeletal muscle profiling assays
209 (**Supplementary Figure 2f**), supporting the idea that C3- and C11-substituted compounds utilize
210 different structural mechanisms and transcriptional networks to modulate GR-mediated
211 phenotypes, which we explore below with molecular dynamics simulations.

212

213 **Gene perturbation studies define underlying causal relationships for GR-mediated skeletal**
214 **muscle phenotypes**

215 We performed gene perturbation studies to determine which correlations are due to causal
216 relationships. The Dex-induced gene, *Fkbp,5* is a good candidate to coordinate metabolic effects
217 of GCs at an organismal level, as its protein product facilitates dephosphorylation of pAKT by the
218 phosphatase, PHLPP1[24]. In addition, Fkbp5 knockout mice show greater skeletal muscle insulin
219 sensitivity and reduced adiposity on a high fat diet[25]. We electroporated *GFP* and either *Fkbp5* or
220 *Foxo1* (an atrophy inducing control gene) expression plasmids into contralateral tibialis anterior
221 (TA) muscles. The *Fkbp5*- or *Foxo1*-transduced muscles were approximately 10% smaller than
222 control (**Figure 3a**). Electroporation with *Foxo1* or *Fkbp5* inhibited insulin-induced *de novo*

223 protein synthesis (**Figure 3b**) and pAKT *in vivo* (**Figure 3c**), demonstrating that *Fkbp5* regulates
224 protein balance in skeletal muscle.

225 Knockdown of NCoR or SMRT (gene names *Ncor1* and *Ncor2*, respectively) enhanced
226 Dex-dependent inhibition of protein synthesis (**Figure 3d, Supplementary Figure 3**), consistent
227 with the peptide binding data showing that GR interaction with NCoR and SMRT corepressor
228 peptides were stimulated by anabolic compounds (**Figure 2b**). In contrast, knockdown of NCOA6
229 and PELP1 fully reversed the inhibitory effect of Dex, while knockdown of SRC2 (gene name
230 *Ncoa2*), but not SRC1 (gene name *Ncoa1*), partially reversed this effect (**Figure 3d**). In contrast,
231 pAKT was regulated by SRC1, as well as PELP1 (**Figure 3e**). These data support a model where
232 GR recruits specific coregulators to distinct subsets of target genes that can have overlapping or
233 different effects on skeletal muscle metabolism and protein balance.

234

235 **Discovery of dissociated GCs with improved skeletomuscular activity profiles**

236 Using our systems chemical biology approach, we developed and characterized compounds that—
237 as a set—showed dissociated effects on glucose disposal and protein balance (**Figure 1**) and
238 identified some unique genes and coregulator interactions associated with these effects (**Figures**
239 **2–3**). We now wanted to ask whether any of the individual compounds showed dissociated effects
240 (see **Supplementary Figure 4** for compound SAR summary or **Supplementary Dataset** for all
241 data) that might have therapeutic potential and identified two promising glucocorticoids with
242 dissociated effects on inflammation and protein balance (**Figure 4a–d**). Three compounds in the
243 C11 series of compounds inhibited IL-6 with efficacies comparable to Dex (**13-15**,
244 **Supplementary Figure 4a**). Among these, SR11466 (**15**) is a partial GR agonist (EC50 = 0.1 nM)
245 that showed no effects on protein balance, and a slight improvement (i.e. less inhibition) compared

246 to Dex in the Glut4 assay (**Figure 4a–d**, **Supplementary Figure 4b**). We also identified SR16024
247 (**18**) as a full GR antagonist (IC50 = 1.4 nM) that stimulated protein synthesis but did not suppress
248 protein degradation or increase Glut4 translocation (**Figure 4b-d**, **Supplementary Figure 4b**).
249 SR11466 and SR16024 increased mitochondrial potential, with the latter doubling mitochondrial
250 potential (**Figure 4e–f**).

251 As a further test for dissociation, the compounds were profiled in primary human
252 osteoblasts for effects on mineralization during 4 weeks of differentiation from mesenchymal stem
253 cells. SR11466 showed a slight improvement in the inhibition of mineralization compared to Dex
254 and PF802, while SR16024 showed a better profile (**Figure 4g**). We also noticed SR15421 (**9**), a
255 lower affinity compound with EC50 of 240 nM (**Supplementary Figure 7a**), that was anti-
256 inflammatory with less impact on mineralization (**Figure 4g-h**). SR15421 is part of the C3-
257 substituted series, where modifying the position of the methyl and the nitrogen on the
258 methylpyridine had profound effects on inhibition of IL-6 secretion (**Figure 4h**). Dose response
259 curves reveal a moderately, but significantly improved effect of SR11466 on mineralization
260 compared to Dex (2-way ANOVA, drug $p = 0.0018$, drug x time $p = 1.4 \times 10^{-4}$), while SR15421
261 and SR16024 inhibited mineralization only at the 10 μM dose (**Figure 4h**). The mineralization
262 data showed very low correlations with the other assays, except for protein synthesis (Pearson $r =$
263 0.54, $p = 4 \times 10^{-3}$), supporting the joint regulation of bone and muscle mass. These data suggest
264 that it is possible to find GCs with improved bone- and muscle-sparing properties compared to
265 Dex using our in vitro profiling platform.

266 We opted to test the two high affinity ligands further in mechanism of action and animal
267 studies, based on their favorable pharmacokinetics (**Supplementary Figure 4c**), and on-target
268 mechanism of action (**Figure 5a–b**, **Supplementary Figure 5**). In vivo, SR11466 strongly

269 suppressed LPS-induced TNFα levels in the blood, while the full antagonist SR16024 was not
270 inhibitory (**Figure 5c**). We also assessed loss of lean mass following a larger dose of LPS, which
271 was significantly worsened by Dex. Both SR11466 and SR16024 were significantly better than
272 Dex, while SR16024 was protective against loss of lean mass compared to vehicle (**Figure 5d**).
273 The differential effects of SR11466 on inflammation and proteostasis demonstrate that it is a bona
274 fide dissociated glucocorticoid, while SR16024 displayed stronger muscle sparing activities.

275 A lactate tolerance test was then administered to probe for differences in liver
276 gluconeogenesis following an overnight fast. Here again, Dex caused significantly greater loss of
277 lean mass after the fast; both SR11466 and SR16024 were significantly better than Dex (**Figure**
278 **5e**); SR16024 attenuated the loss of overall body weight (**Figure 5f**). The lactate tolerance test
279 showed that both Dex and SR11466 increased the rate of glucose production, while SR16024 did
280 not (**Figure 5g**), suggesting that ligand-specific GC effects on glucose uptake in skeletal muscle
281 and gluconeogenesis in the liver may utilize common signaling mechanisms, such as ligand-
282 selective coregulator recruitment, to integrate organismal stress responses.

283

284 **Molecular dynamics simulations revealed that suppression of IL-6 is associated with specific**
285 **structural perturbations.**

286 To understand how substitutions to the C3 position regulate allosteric signaling in GR, we
287 performed all atom molecular dynamics (MD) simulations comparing **7** and **9**, which differ only
288 in the placement of the methyl on the pyridine (**Figure 1g**) but showed very different effects on
289 suppression of IL-6 (**Figure 4h**). Molecular docking demonstrated that the compounds bound
290 similarly to Dex, with the pyridine extending off the A-ring into a solvent channel, in between
291 helix 3 (h3) and h5 (**Supplementary Methods**, **Supplementary Figure 6a**). In three independent

292 1 μs simulations of ligand-bound and ligand-free (apo) GR LBD, we observed no significant
293 structural changes in the conformation of helix 12 (h12). However, ligand anti-inflammatory
294 activity (Dex > **9** >**7** > apo) was associated with a multi-Å decrease in the distance between the C-
295 terminus of h11 and the N-terminus of h3, and a decrease in the heterogeneity of this h3/h11
296 interface (**Figure 6a–c**). We also assessed patterns of correlated motion and found that the **7**
297 showed less correlation between residues h3 and h11/h12 residues compared to dex, with 9 again
298 showing intermediate effects (**Supplementary Figure 6b**).

299 To further probe for effects of the C3 substitutions on correlated motion between h12 and
300 the solvent channel, we used dynamical network analysis[26] of ligand-free and the ligand-bound
301 complexes by connecting pairs of nodes with their edges if they have satisfied a distance
302 requirement (<4.5 Å) for at least 75% of the simulation time. Edge distance is inversely
303 proportional to the pairwise correlations between two nodes; thus, a short path length indicates a
304 strong correlation/communication. A pair of distal nodes are connected by the optimal (shortest)
305 path and the suboptimal (longer) paths with the length defined as the sum of edge distances along
306 the path. We analyzed the top 1000 suboptimal paths between residue E755 and R614 as two nodes
307 to study the allosteric communication between h12 and the C-terminus of h5, where the
308 modifications on the steroidal A ring extend to the solvent channel. With apo GR, this
309 communication was through h11 and along h5, while with dex it wrapped around the ligand
310 binding pocket from h12 to h3 and then through the β-sheet (**Figure 6d**), enabled by the dex-
311 induced closing of the distance between h3 and h11 (**Figure 6b**). With Dex, this was associated
312 with much longer path lengths (**Figure 1e**), representing weaker allosteric communication overall.
313 With **9**, there were less of these extended path lengths, while **7** more closely resembled the apo
314 GR (**Figure 6d-e**). An analysis of residues contacting the C3-substituted pyridine showed that

315 differential positioning of the R611 side chain on h5, which can form h-bonds with the pyridine or
316 A-ring ketone of Dex, can drive the orientation of the steroid core to control the dynamics and
317 surface structure and associated receptor activity (**Figure 6f–g, Supplementary Figure 6c–e**).
318

319 **Discussion**

320 In this work, we used a structure-based design strategy and LCA to reveal how GCs can use
321 different coregulators and transcriptional networks for the physiological control of glucose
322 disposal and protein balance during acute nutrient deprivation. By examining closely related
323 compounds with LCA, we determined that protein balance and mitochondrial potential were
324 intercorrelated but dissociated from Glut4 translocation and suppression of IL-6. Using a
325 physiologically relevant skeletal muscle profiling platform optimized to study insulin signaling
326 during nutrient deprivation, we were able to identify SR11466 as a partial GR agonist that was not
327 catabolic, demonstrating in vivo dissociated anti-inflammatory activity. In fact, SR11466 was
328 slightly anabolic for protein balance, while maintaining strong anti-inflammatory activity in vivo.
329 Such compounds may be useful treatments for cachexia, muscular dystrophies, back pain or
330 osteoarthritis. We also identified SR16024 as a highly anabolic GC that inhibits both fasting- and
331 LPS-induced weight loss, while stimulating mitochondrial potential and protein synthesis in
332 response to insulin. Further studies are needed to evaluate the long term effects of SR16024, but
333 GR antagonists have been tested clinically for depression[27], and may have efficacy in muscular
334 dystrophies and enzalutamide-resistant prostate cancers that have switched from androgen to
335 glucocorticoid dependency[28]. While preliminary, the lack of SR15421 effects on mineralization
336 suggests that it may also be possible to dissociate the anti-inflammatory and osteoporotic effects
337 of GCs.

338 The unbiased nature of LCA enabled the identification of a number of unexpected signaling
339 and biophysical properties of GR. Insulin receptor signaling pathways control both anabolic and
340 catabolic signaling, and these can be dissociated by transcriptional control of pathway-selective
341 regulators, often with very subtle changes in gene expression. Covariance among assays reflects
342 common underlying signaling mechanisms driven by common receptor conformations,
343 coregulators, and target genes. The correlation between effects on bone and skeletal muscle was
344 not surprising, but the connection between anti-inflammatory and metabolic effects of GCs in
345 different cell types was unexpected and may point to an organismal level of evolutionary
346 connection between underlying signaling pathways. GC coordination of the inflammatory
347 response often coincides with immune differentiation[29,30], which requires metabolic adaptations
348 [31,32]. This suggests that GCs may use a common set of coregulators to coordinate anti-
349 inflammatory effects with modulation of metabolism. LCA provides a mechanism to identify
350 common signaling mechanisms among different cell types and processes.

351 GC-regulated transcription is controlled via underlying biophysical properties of GR, such
352 as oligomerization, nuclear translocation, and on/off rates of interactions with an ensemble of
353 response elements, coregulators, and collaborating transcription factors. We have shown here that
354 LCA predicts that ligand-selective surface conformers—identified from a structural peptide
355 interaction assay—can predict differential effects of the ligands, which we validated with
356 knockdown of selected coregulators. We and others have observed a similar dichotomy where
357 Ncoa2/SRC2/GRIP1 is required for NF-κB-induced cytokine production, but then switches to a
358 repressor upon recruitment of GR to the promoter[33,34], representative of a more general phenomena
359 of receptors using many coregulators to regulate a single gene, but also some shared and some
360 differential coregulator usage across genes[14,35,36]. The selective association of GR nuclear

361 translocation with glucose disposal and not protein balance was also surprising. It suggests that
362 GCs modulate insulin dependent Glut4 translocation via a graded transcriptional program that is
363 highly sensitive to the amount of nuclear GR, and control protein balance through transcriptional
364 responses that require a threshold amount of nuclear GR. This is consistent with other data
365 suggesting that only 10% of GR may be DNA-bound at any given time [37]. Similarly, we previously
366 found that the mammalian two-hybrid assay was a much better predictor of proliferation by
367 estrogen receptor ligands than a chromatin immunoprecipitation assay [9], suggesting that complex
368 biology can be simulated by a set of simple biophysical models and their importance identified
369 with LCA.
370
371 **References**
372

373 1. Watson, M.L. et al. A cell-autonomous role for the glucocorticoid receptor in skeletal
374 muscle atrophy induced by systemic glucocorticoid exposure. Am J Physiol Endocrinol Metab
375 302, E1210-20 (2012).
376 2. Bodine, S.C. & Furlow, J.D. Glucocorticoids and Skeletal Muscle. Adv Exp Med Biol 872,
377 145-76 (2015).
378 3. Nettles, K.W. & Greene, G.L. Ligand control of coregulator recruitment to nuclear
379 receptors. Annu Rev Physiol 67, 309-33 (2005).
380 4. Kuo, T. et al. Genome-wide analysis of glucocorticoid receptor-binding sites in myotubes
381 identifies gene networks modulating insulin signaling. Proc Natl Acad Sci U S A 109, 11160-5
382 (2012).
383 5. Chen, S.L., Dowhan, D.H., Hosking, B.M. & Muscat, G.E. The steroid receptor
384 coactivator, GRIP-1, is necessary for MEF-2C-dependent gene expression and skeletal muscle
385 differentiation. Genes Dev 14, 1209-28 (2000).
386 6. Tobimatsu, K. et al. Overexpression of the transcriptional coregulator Cited2 protects
387 against glucocorticoid-induced atrophy of C2C12 myotubes. Biochem Biophys Res Commun 378,
388 399-403 (2009).
389 7. Amat, R., Solanes, G., Giralt, M. & Villarroya, F. SIRT1 is involved in glucocorticoid-
390 mediated control of uncoupling protein-3 gene transcription. J Biol Chem 282, 34066-76 (2007).
391 8. Nwachukwu, J.C. et al. Systems Structural Biology Analysis of Ligand Effects on ERalpha
392 Predicts Cellular Response to Environmental Estrogens and Anti-hormone Therapies. Cell Chem
393 Biol 24, 35-45 (2017).
394 9. Nwachukwu, J.C. et al. Predictive features of ligand-specific signaling through the estrogen
395 receptor. Mol Syst Biol 12, 864 (2016).
396 10. Srinivasan, S. et al. Ligand-binding dynamics rewire cellular signaling via estrogen
397 receptor-alpha. Nat Chem Biol 9, 326-32 (2013).

398 11. Jin, Z. et al. Synthesis of novel steroidal agonists, partial agonists, and antagonists for the
399 glucocorticoid receptor. Bioorg Med Chem Lett 27, 347-353 (2017).
400 12. Hu, X. et al. The antagonists but not partial agonists of glucocorticoid receptor ligands
401 show substantial side effect dissociation. Endocrinology 152, 3123-34 (2011).
402 13. Stock, T., Fleishaker, D., Wang, X., Mukherjee, A. & Mebus, C. Improved disease activity
403 with fosdagrocorat (PF-04171327), a partial agonist of the glucocorticoid receptor, in patients with
404 rheumatoid arthritis: a Phase 2 randomized study. Int J Rheum Dis (2017).
405 14. Nwachukwu, J.C. et al. Resveratrol modulates the inflammatory response via an estrogen
406 receptor-signal integration network. Elife 3, e02057 (2014).
407 15. Aarts, J.M. et al. Robust array-based coregulator binding assay predicting ERalpha-agonist
408 potency and generating binding profiles reflecting ligand structure. Chem Res Toxicol 26, 336-46
409 (2013).
410 16. Geiss, G.K. et al. Direct multiplexed measurement of gene expression with color-coded
411 probe pairs. Nat Biotechnol 26, 317-25 (2008).
412 17. Stitt, T.N. et al. The IGF-1/PI3K/Akt pathway prevents expression of muscle atrophy-
413 induced ubiquitin ligases by inhibiting FOXO transcription factors. Mol Cell 14, 395-403 (2004).
414 18. Goodyear, L.J. & Kahn, B.B. Exercise, glucose transport, and insulin sensitivity. Annu Rev
415 Med 49, 235-61 (1998).
416 19. Magomedova, L. & Cummins, C.L. Glucocorticoids and Metabolic Control. Handb Exp
417 Pharmacol 233, 73-93 (2016).
418 20. Kuo, T., Harris, C.A. & Wang, J.C. Metabolic functions of glucocorticoid receptor in
419 skeletal muscle. Mol Cell Endocrinol 380, 79-88 (2013).
420 21. Breiman. Random Forests. Machine Learning 45, 5-32 (2001).
421 22. Kursa, M.B. Robustness of Random Forest-based gene selection methods. BMC
422 Bioinformatics 15, 8 (2014).
423 23. Luciani, D.S. et al. Bcl-2 and Bcl-xL suppress glucose signaling in pancreatic beta-cells.
424 Diabetes 62, 170-82 (2013).
425 24. Pei, H. et al. FKBP51 affects cancer cell response to chemotherapy by negatively
426 regulating Akt. Cancer Cell 16, 259-66 (2009).
427 25. Balsevich, G. et al. Stress-responsive FKBP51 regulates AKT2-AS160 signaling and
428 metabolic function. Nat Commun 8, 1725 (2017).
429 26. Bowerman, S. & Wereszczynski, J. Detecting Allosteric Networks Using Molecular
430 Dynamics Simulation. Methods Enzymol 578, 429-47 (2016).
431 27. Block, T. et al. Mifepristone Plasma Level and Glucocorticoid Receptor Antagonism
432 Associated With Response in Patients With Psychotic Depression. J Clin Psychopharmacol 37,
433 505-511 (2017).
434 28. Arora, V.K. et al. Glucocorticoid receptor confers resistance to antiandrogens by bypassing
435 androgen receptor blockade. Cell 155, 1309-22 (2013).
436 29. Yu, B. et al. Epigenetic landscapes reveal transcription factors that regulate CD8(+) T cell
437 differentiation. Nat Immunol 18, 573-582 (2017).
438 30. Coppo, M., Chinenov, Y., Sacta, M.A. & Rogatsky, I. The transcriptional coregulator
439 GRIP1 controls macrophage polarization and metabolic homeostasis. Nat Commun 7, 12254
440 (2016).
441 31. Geltink, R.I.K., Kyle, R.L. & Pearce, E.L. Unraveling the Complex Interplay Between T
442 Cell Metabolism and Function. Annu Rev Immunol 36, 461-488 (2018).

32. Van den Bossche, J., O'Neill, L.A. & Menon, D. Macrophage Immunometabolism: Where Are We (Going)? Trends Immunol 38, 395-406 (2017).
33. Hudson, W.H. et al. Cryptic glucocorticoid receptor-binding sites pervade genomic NF-kappaB response elements. Nat Commun 9, 1337 (2018).
34. Chinenov, Y. et al. Role of transcriptional coregulator GRIP1 in the anti-inflammatory actions of glucocorticoids. Proc Natl Acad Sci U S A 109, 11776-81 (2012).
35. Stallcup, M.R. & Poulard, C. Gene-Specific Actions of Transcriptional Coregulators Facilitate Physiological Plasticity: Evidence for a Physiological Coregulator Code. Trends Biochem Sci 45, 497-510 (2020).
36. Stashi, E., York, B. & O'Malley, B.W. Steroid receptor coactivators: servants and masters for control of systems metabolism. Trends Endocrinol Metab 25, 337-47 (2014).
37. Voss, T.C. et al. Dynamic exchange at regulatory elements during chromatin remodeling underlies assisted loading mechanism. Cell 146, 544-54 (2011).
38. Heikkinen, S., Argmann, C.A., Champy, M.F. & Auwerx, J. Evaluation of glucose homeostasis. Curr Protoc Mol Biol Chapter 29, Unit 29B 3 (2007).
39. Bruno, N.E. et al. Creb coactivators direct anabolic responses and enhance performance of skeletal muscle. EMBO J 33, 1027-43 (2014).
40. Hong, D.H. & Forsberg, N.E. Effects of dexamethasone on protein degradation and protease gene expression in rat L8 myotube cultures. Mol Cell Endocrinol 108, 199-209 (1995).
41. Walker, D., Htun, H. & Hager, G.L. Using inducible vectors to study intracellular trafficking of GFP-tagged steroid/nuclear receptors in living cells. Methods 19, 386-93 (1999).
42. Stavreva, D.A. et al. Prevalent glucocorticoid and androgen activity in US water sources. Sci Rep 2, 937 (2012).

Acknowledgements. N.E.B. was supported by the BallenIsles Men's Golf Association. K.W.N. is supported by G.S. Humane Corp. W.M. Keck Foundation Grant to EAO.

Author contributions. Conceptualization, N.E.B. and K.W.N.; Methodology, N.E.B., K.W.N., S.V.B, J.C.N., G.L.H., M.C., R.H.; Investigation, N.E.B., S.S., S.V.B., J.C.N., C.C.N., D.A.S., R.H., D.J.K., X.L., O.E., Z.J., T.M.K.; Resources, Z.J., T.M.K.; Writing – Original Draft, K.W.N., N.E.B., J.C.N.; Writing–revision, K.W.N., J.C.N., X.L., E.A.O., D.J.K, E.O.; Supervision, K.W.N., N.E.B., G.L.H., T.M.K., E.A.O., T.I.

Methods

Quantification and Statistical analyses

All statistics were done using GraphPad Prism unless otherwise stated. Random Forest/Boruta were done with R. For Pearson correlation, the p-value (two-tail) tested the null hypothesis that the true population correlation coefficient for that pair of variables is zero. Two-tailed unpaired Student's t-test was done to compare only two groups. One-way or two-way ANOVA was used for comparisons of more than two groups with correction for multiple hypothesis testing. All values were expressed as the mean ± S.E.M. The compound injections were done by one person and the determination of weight/body composition done by another person blinded to the treatment groups. For the high content imaging assay of myotube diameter and the in cell western blots, images were visually inspected in a blinded fashion for the presence of intense foci or speckles and those images were not included in the analyses. For the IL-6 dose curves, data were identified through the linear regression function in GraphPad Prism

Machine learning

A decision tree-based classification algorithm, *random forest*, can be used to divide the data into subsets many times to create a forest of many classifications, and determine which classification best explains the data [21]. This produces a rank order of features (i.e. the assays) that predict the dependent variable but does not provide a statistical cut-off that indicates which features are important. The Boruta algorithm resolves this issue by creating shuffled copies of the features and evaluates the degree to which random forest performs better on the real data compared to the shuffled data [22].

After scaling the full dataset to Z scores, the *Boruta* package was used to identify predictors of GR-regulated phenotypes. Each Boruta prediction was performed with three different random

501 seeds, the results of which were then compiled. Variables that were confirmed in 2 or more runs
502 were selected as predictors. The minimal or best predictive model was obtained using the
503 *randomForest* package. To this end, predictors were added to the model one-by-one, in order of
504 importance. Each model was assessed by growing 500 decision trees and testing one predictor at
505 each tree branch. If a predictor improves the predictive power of model, it is retained in the model.
506 If a predictor fails to improve the model it is discarded, before the next predictor is tested. This
507 process is repeated until the last predictor is tested. The best model therefore consists of only the
508 minimal set of predictors. Sample *R* scripts are available at:
509 https://github.com/jnwachuk/Ligand_Class_Analysis_Reveals_Dissociated_Signaling_Networks
510 _in_Skeletal_Muscle.
511

512 **Animals**

513 All animal procedures were approved by the Scripps Research Institute IACUC. Male C57BL/6J
514 mice, 8–10 wk old, were acquired from the Jackson Laboratories (Bar Harbor, ME) and used for
515 all conditions. Mice were housed under a 12-h light/dark cycle with *ad libitum* access to food and
516 water unless otherwise stated. Before all surgical procedures, mice were anesthetized with gaseous
517 isoflurane (Baxter, USP, USA). Before tissue extraction, the mice were euthanized with CO_2 and
518 cervical dislocation.

519 ***In vivo LPS assay***

520 Mice were treated with 1.5 μg LPS (Sigma L2880) for 1 hr and then blood drawn for determination
521 of TNFα (ELISA, R&D Systems, MTA00B). Mice were then given an injection of 30 μg LPS for
522 23 hrs. Body composition was determined using time domain nuclear magnetic resonance (TD-
523 NMR) in a Bruker minispec.

524 ***Lactate tolerance test***

525 Mice were administered GCs at 10 mg/kg IP and then fasted overnight. The next morning
526 lactate (1.5 g/kg) was injected intraperitoneally and blood glucose assayed at the indicated times
527 with an Accu-check glucose monitor as described[38].

528 ***Electric-pulse-mediated gene transfer and in vivo SUnSET assay***

529 Plasmid DNA (50 μg) was transfected into mouse tibialis anterior (TA) muscles by electroporation
530 as described previously [39]. 1 hr before electroporation mice were anesthetized, and a small incision
531 was made through the skin covering the TA muscle and then injected with 30 Al of 0.5 U/Al
532 hyaluronidase and then injected with plasmid DNA. *Fkbp5* and *Foxo1* expression plasmids were
533 from the MGC Expression Ready cDNA Library Plasmid DNA was grown in DH5 *Escherichia*
534 *coli*, purified with an EndoFree plasmid kit (Qiagen, Valencia, CA, USA), and resuspended in 71
535 mM sterile PBS. After the injections, electric pulses were administered by using non-invasive
536 platinum-coated tweezertrodes. Eight 100-ms square-wave electric pulses at a frequency of 1 Hz
537 and at 200-ms intervals were delivered with an ECM 830 electroporation unit (BTX-Harvard
538 Apparatus, Holliston, MA, USA) with a field strength of 40 V/cm. After the electroporation
539 procedure, the incision was closed with Vetbond surgical glue. At 7 d after transfection, muscles
540 were subjected to nonradioactive *in vivo* measurements of protein synthesis. mice were
541 anesthetized as described above and then given an intraperitoneal injection of 0.040 mol/g
542 puromycin dissolved in 100 μl of PBS. At exactly 30 min after injection, tissues were extracted
543 and frozen in liquid N_2 for WB analysis.

544

545 **Western blot analysis**

546 Whole cell extracts were prepared in HEPES whole cell lysis buffer (20 mM HEPES, pH 7.4, 1%

547 TX-100,1x phosphoSTOP complete inhibition cocktail tablets [Roche], and 1X Complete EDTA-
548 Free protease inhibitor cocktail [Roche]). Frozen muscle tissue was homogenized in lysis buffer
549 T-PER® Tissue Protein Extraction reagent (Thermo Scientific) by a polytron homogenizer and
550 sonication. The protein concentration was determined using the protein assay reagent (Bio-Rad).
551 Sixty to eighty μg of protein was separated by SDS-PAGE and transferred to nitrocellulose
552 membranes for immunoblotting.
553

554 **Cell Culture and screening assays**

555 C2C12 myoblasts, L6 myoblasts, and A549 cells (ATCC) were cultured in high glucose DMEM
556 supplemented with glutamine and 10% FBS. For steroid-free culture conditions, cells were grown
557 in charcoal:dextran-stripped FBS (Gemini Bio-products, cat no. 100-119).

558 ***Optimization of culture conditions for GR ligand assays***

559 Our goal was to develop assays that replicate the in vivo effects of GCs at low nM doses, not the
560 50-100 μM doses that have been reported as necessary to induce atrophy in vitro. We noticed that
561 Dex strongly inhibits myoblast proliferation, and promotes fusion into myotubes, and thus we
562 might expect the test compounds to have differential effects on differentiation, with agonists
563 producing a more fully developed and mature network of myotubes, which are then subject to GC
564 mediated atrophy of the myotubes. To avoid such effects on myogenesis, we switched myoblasts
565 to differentiation media, and then on day 4, added 10 μM cytarabine, a chemotherapy agent that
566 kills dividing cells, and then adding GCs on day 6 or 7 and completing assays on day 8.

567 We also hypothesized that GCs would induce atrophy more readily in the normal
568 physiological context, nutrient deprivation. We optimized the timing of nutrient deprivation and
569 administration of GCs to obtain the best signal to noise ratio of Dex vs vehicle. We were initially

570 unable to observe much effect on pAKT, because it was elevated basally. This was optimized by
571 adding an hr of serum free treatment. Adding an insulin challenge increased the signal to noise in
572 all the assays and focused the experimental design on GC regulation of the insulin signaling
573 pathways effects on protein balance and glucose disposal. Variation was further reduced by use of
574 a BioMek 100-nl pin-tool dispensing robot and using a series of partial media changes to prevent
575 cells from detaching. To reduce edge effects and media evaporation over the 8 days of the assays
576 we added a gas permeable membrane to the 384-well plates for all assays except the protein
577 degradation assay. All assays were performed in C2C12 cells (ATCC) except for the Glut4
578 translocation assay, which was performed in rat L6 myocytes. This is because the C2C12 have
579 upregulated Glut1, which is constitutively active, and overwhelms any insulin-induced effects on
580 Glut4 translocation. Assays were optimized until the they could be repeated with a Pearson
581 correlation > 0.8 between biological replicates from separate passages of cells.

582 ***Optimized protocol***

583 On the day of the experiments cell were seeded at 70% confluency and 48 hrs latter washed with
584 PBS and switch to differentiation media consisting of phenol-free DMEM supplemented with
585 glutamine and charcoal stripped serum (Sigma 18l289). Partial media changes were performed
586 every 48 hrs to prevent lifting of the tubes from the wells. After six days in differentiation media,
587 the cells were serum starved, treated with ligands and used as described on each particular assay.
588 348-well plates were used unless otherwise noted, and a gas permeable sealing membrane
589 (Breathe-Easy membrane) was applied immediately after seeding and replaced after every partial
590 media change.

591 ***Glut4 translocation assay***

592 Low passage, L6 rat myoblast (ATCC), were cultured in high glucose DMEM supplemented with

593 glutamine and 10% serum (proliferation media). On day 1 of differentiation, 2,500 cells were
594 seeded on 384-well plates in 50 μl of proliferation media that was replaced every other day. On
595 day 5 cells were washed and replaced with differentiation media, which was then replaced daily.
596 After 3 days of differentiation the cells were ligand treated and serum starved overnight. Next day
597 we replace the medium with 100 μl DMEM ± 1 μM insulin (Sigma I0516) without serum or
598 glucose and incubate for 1 hour and then fixed with 3.7% formaldehyde for 20 minutes. Non-
599 permeabilized cell were then washed in TBS and blocked for 2 hours (Rockland MB-070) then
600 incubated in primary anti-Glut-4 antibody in blocking buffer for 48 hours at 4 °C. Then the plates
601 were washed 5 times for 5 minutes with TBS-T and then incubated with secondary antibody for 1
602 hr wash and analyzed using a LI-COR Odyssey imaging system.

603 ***SUnSET assay for insulin-mediated protein synthesis***

604 C2C12 myoblasts were cultured and differentiated in 384-well plates as described above. After
605 differentiation, the different ligands were added with a Biomek pin tool dispenser in serum-free
606 DMEM overnight, next treated with 100 nM insulin. After 60 min, 1 μM puromycin was added to
607 all wells, and the cells were incubated for an additional 30 min. The in cell western (LI-COR) was
608 used to quantitate uptake of puromycin. Cells were fixed with 3.7% formaldehyde for 20 minutes.
609 Non-permeabilized cell were then washed in TBS and blocked for 2 hours (Rockland MB-070)
610 then incubated in primary anti-puromycin antibody in blocking buffer for 48 hours at 4 °C. Then
611 the plates were washed 5 times for 5 minutes with TBS-T and then incubated with secondary
612 antibody for 1 hr wash and analyzed using a LI-COR Odyssey imaging system.

613 .

614 ***Protein degradation***

615 Rates of protein degradation were determined by measuring the release of TCA-soluble

616 radioactivity from proteins prelabeled with [3H]-phenylalanine. In brief C2C12 cells were seed in
617 24 well plates and after completing differentiation, myotubes were labeled with 1.0 µCi/ml of L-
618 [3,5-3H]- phenylalanine for 48 h dedifferentiation media. Cells were then treated for 24 h with
619 ligands in DMEM containing 2 mM unlabeled phenylalanine. After treatment, the culture medium
620 was transferred into a microcentrifuge tube containing 100 µl of bovine serum albumin (10 mg/ml)
621 and TCA was added to a final concentration of 10% (w/v). Samples were incubated at 4° C for 1
622 hr followed by centrifugation for 5 min. The supernatant was used for determination of TCA-
623 soluble radioactivity. The protein precipitates were dissolved with a tissue solubilizer
624 (Solvable™). Cell monolayers were washed with ice-cold PBS and solubilized with 0.5 M NaOH
625 containing 0.1% Triton X-100. Radioactivity in the cell monolayer and TCA soluble and insoluble
626 fractions were measured using a Packard TRI-CARB 1600 TR liquid scintillation analyzer. Protein
627 degradation was expressed as the percentage protein degraded over the 24 hr period and was
628 calculated as 100 times the TCA-soluble radioactivity in the medium divided by the TCA-soluble
629 plus the TCA-insoluble radioactivity in the medium plus the cell layer (i.e., myotube) radioactivity
630 [40].

631 ***High-content imaging and analysis***

632 Primary or C2C12 myotubes or mycocytes in black 96- or 384-well tissue culture plates with clear
633 bases (Greiner Bio-One, North America, Inc.) were stained for 15 min with 200 nM MitoTracker®
634 Orange CM-H_2TMRos dye (Invitrogen™ by ThermoFisher Scientific) for imaging of
635 mitochondrial potential. The cells were rinsed with steroid-free DMEM to remove un-incorporated
636 dye, and then incubated in the differentiation media for 45 min to reach peak fluorescence. Cells
637 were fixed in 4% formaldehyde for 20 min, stained with 300 nM DAPI for 5 min, permeabilized
638 in PBS containing 0.1% Triton X-100 for 20 min, blocked for 1 h with 1x TBS containing 0.1%

639 Tween-20 (TBS-T) and 2.5% normal goat serum, and incubated at 4 °C overnight with an
640 AlexaFluor® 488-conjugated anti-skeletal muscle myosin (F59) antibody (Santa Cruz
641 Biotechnology, Inc. cat no. sc-32732 AF488). The next day, the myotubes were washed 4 times
642 with TBS-T to remove unbound antibodies and rinsed twice with PBS. The stained myotubes were
643 imaged at 10–20X magnification on the IN Cell Analyzer 6000 platform (GE Healthcare). For
644 each treatment condition, a stack of 24–27 images containing an average of 50–100 myotubes per
645 image were analyzed using the IN Cell Developer Toolbox image analysis software, with a
646 customized segmentation protocol for myotubes. The average (mean) diameter and mitochondrial
647 potential (i.e. MitoTracker staining density x area) of myotubes in these images were then
648 calculated.

649 ***Nuclear translocation***

650 The cell line used for these experiments (3617) expresses green fluorescent protein (GFP)-tagged
651 GR (GFP-GR) from a chromosomal locus under control of the tetracycline-repressible promoter
652 [41]. Cytoplasm-to-nuclear translocation of the GFP-GR in response to different compounds was
653 determined as previously described [42]. Cells were plated on a 384-well plate in DMEM medium
654 containing 10% charcoal stripped serum (Hyclone, Logan, UT) without tetracycline (to allow the
655 expression of the GFP-GR) at density of 2,500 cells per well. Cells were treated with compounds
656 or a diluent as control for 30 min, fixed with paraformaldehyde, the nuclei stained with 4′,6-
657 diamindino-2-phenylindole (DAPI) and Perkin Elmer Opera Image Screening System was used
658 for fully automated collection of images. An image analysis pipeline was customized using the
659 Columbus software (PerkinElmer) to automatically segment the nucleus using the DAPI channel
660 and then construct a ring region (cytoplasm) around the nucleus mask for each cell in the digital
661 micrographs. Translocation was calculated as a ratio of the mean GFP-GR intensity in nucleus and

662 cytoplasm, and each value was further normalized to the value for the control (i.e., DMSO) sample
663 on the same plate.

664 ***Osteogenic Differentiation of Human Mesenchymal Stem Cells***

665 Human MSCs at passage 2 were maintained in growth media consisted of alpha-MEM (Life
666 Technologies, 32561--037) supplemented with 17% FBS (Sigma-Aldrich, 12303C), 2mM L-
667 glutamine (Life Technologies, 25030-081), and 100 units/mL penicillin/streptomycin (Life
668 Technologies, 15140-122). Effect of glucocorticoid receptor modulators on osteogenic
669 differentiation of MSCs was quantified using Alizarin Red S (Sigma-Aldrich, A5533) staining.
670 Briefly, human MSCs were seeded in the middle 8 wells of 48-well plates at plating density of
671 10,000 cells per well. PBS (Life Technologies, 10010-031) was added to surrounding wells to
672 reduce evaporation of media in the middle wells during prolonged incubation. 24h later, growth
673 media was replaced by osteogenic induction media (OIM) consisted of low-glucose DMEM (Life
674 Technologies, 10567-014) supplemented with 10% FBS (Sigma-Aldrich, 12303C), 50 µg/ml L-
675 ascorbic-2-phosphate (Sigma-Aldrich, A8960), 10mM β-glycerolphosphate (Sigma-Aldrich,
676 G9891), and glucocorticoid modulators. OIM containing test compounds was replaced every
677 week. At the end of 2 weeks, monolayers were washed with PBS (Life Technologies, 10010-031),
678 incubated in Richard-Allan Scientific™ Neutral Buffered Formalin (10%) (Thermo Scientific,
679 5725) for 2 h at room temperature, washed with deionized water and stained with Alizarin Red S
680 for 30 min at room temperature. Monolayers were then rinsed 3 × with deionized water until clear,
681 stain was then extracted with 10% (w/v) cetylpyridinium chloride (Sigma-Aldrich, C0732) in
682 10 mM sodium phosphate (Sigma, S5011 and S5136), pH 7.0 for 15 min at room temperature and
683 the amount of extracted dye quantified spectroscopically at 562 nm. Spectroscopic analysis
684 performed using a synergy™ NEO HTS Multi-Mode Microplate Reader (BioTek Instruments,

685 Inc.).

686 ***IL-6 secretion***

687 IL-1β (R&D systems) was dissolved in phosphate-buffered saline plus 0.1% bovine serum albumin
688 (Sigma). A549 cells were plated in DMEM containing charcoal stripped serum in 384 well plates.
689 The next day, cells were treated for 24 with GCs at 1 μM and then treated with 1 ng/ml IL-1β for
690 24 hrs. supernatants were collected and IL-6 assayed with AlphaLISA (PerkinElmer) using the
691 manufacturer's instructions.

692

693 **Micro array Assay for Real-time Coregulator-Nuclear receptor Interaction (MARCoNI)**

694 This method has been previously described [15]. Assay mixes with 1 nM GST-tagged GR (aa 521-
695 777, Invitrogen #PV4689), 25 nM Alexa-488 conjugated GST antibody (Fisher Scientific,
696 #10368552), 5 mM DTT, in Coregulator buffer F (Invitrogen, #PV4547) in the presence of solvent
697 only (2% DMSO) or 1 μM compound as indicated, were prepared on ice. Experiments were
698 conducted on a PamStation96 (PamGene) using 2 cycles per minute at room temperature. In short,
699 PamChip arrays (PamGene #88101) were blocked for 20 cycles with 1% Bovine serum albumin
700 (Calbiochem #126609) in Tris-buffered saline (TBS), incubated for 40 minutes with 25 μl assay
701 mix using 3 arrays per mix and finally rinsed twice with TBS. Binding on array (tif) images were
702 quantified with BioNavigator software (PamGene). A modulation index, i.e. the log-transformed
703 ratio of binding in presence over absence (solvent) of compound, was calculated for each
704 interaction. Significance of the modulation was assessed using Student's t-Test and FDR post hoc
705 correction.

706

707

708 **Antibodies**

709 Anti-puromycin antibody: 3RH11 (Kerafast, Inc. cat no. EQ0001), or clone 4G11
710 (MilliporeSigma, cat no. MABE342). Anti-AMPKα Antibody (Cell Signaling Technology, Inc.
711 #2532). Phospho-AMPKα (Thr172) (40H9) (Cell Signaling Technology, Inc. #2535), Anti-AKT1
712 (2H10) antibody (Cell Signaling Technology, Inc. #2967), Anti-pAKT-T308 (C31E5E) antibody
713 (Cell Signaling Technology, Inc. #2965)

714

715 **Lentiviral vectors and transduction**

716 Lentiviruses were produced from sets of four mouse piLenti-siRNA-GFP lentiviral vectors
717 (Applied Biological Materials, Inc. Richmond, BC, Canada) targeting *Pelp1* (cat no.
718 i029598), *Ncoa2* (cat no. i033105), *Ncoa1* (cat no. i038883), *Ncoa6* (cat no. i042804), *Ncor1* (cat
719 no. i044954), or *Ncor2* (cat no. i042611), or the Control piLenti-siRNA-GFP lentiviral vector (cat
720 no. LV015-G). HEK-293T cells in 3x 10 cm dishes per construct, were co-transfected with 10 µg
721 lentiviral vector, 7.5 µg psPAX2, and 2.5 µg pVSV-G per dish using ProFection® kit (Promega)
722 according to manufacturer's protocol. At ~15 h post-transfection, the media was replaced with 2.5
723 ml fresh media. Conditioned media containing lentiviral particles (LVM) were collected every 12
724 h for another 48 h, pooled, and stored at 4 °C. LVM were passed through a 0.45-micron filter to
725 remove cell debris, and then centrifuged at 4,000 RPM overnight to pellet the viruses. The pellets
726 were resuspended in 50 µl sterile PBS and added with 8 µg/ml polybrene to day-1 C2C12
727 myoblasts.

728

729

730

731 **Figure Legends**

732 **Figure 1. Structure-based design approach and glucocorticoid profiling platform.**

733 **a**) Chemical structure of the dissociated glucocorticoid, PF802.

734 **b**) Crystal structure of the dexamethasone (Dex) bound GR ligand-binding domain (LBD). Helix
735 12 is colored red and the SRC2 coregulator peptide binding in the AF2 binding surface is colored
736 coral. Carbons-3, -11, and -17 are indicated in the chemical structure (1M2Z.pdb).

737 **c**) The bulky dimethylanaline group attached at C11 in RU-486 displaces h12 from the agonist
738 position to disrupt the AF2 surface and generate antagonism (1NHZ.pdb).

739 **d**) Substitutions at C3, as seen with the furoate group in momethasone furoate or the propyne in
740 RU-486 target a small internal pocket to increase affinity (4P6W.pdb).

741 **e**) Substitutions at C3 of the steroidal A-ring enter the solvent channel underneath the AF2 surface,
742 potentially changing the shape of the surface and the ensemble of interacting coregulators
743 (3BQD.pdb).

744 **f**) Model of SR11466 (**15**) bound to the GR LBD

745 **g**) Glucocorticoids used in this study.

746 **h**) Compound profiling and computational strategy. Effects on the independent variables were
747 used in a machine learning approach, Random Forest, to identify predictors of skeletal muscle
748 phenotypes, the dependent variables, described in **Figure 2** and below.

749 **i**) Relationships among GR-mediated phenotypes. Lines indicate significant Pearson correlation
750 between variables using Bonferroni $p_{Adj} < 0.0071$.

751

752 **Figure 2. Machine learning reveals best predictors of selective modulation and common**
753 **signaling**

754 **a**) Compounds **1-3**, **6-27** were profiled for regulation of specific target genes in skeletal muscle
755 and GR interaction with specific peptides. Predictors of GR-mediated phenotypes were identified
756 using the random forest classifier[21,22] and statistical thresholds established with the Boruta wrapper
757 algorithm for feature selection[22]. The numbers following the peptide names represent the amino
758 acid beginning of the peptide from the full-length protein.
759 **b**) Predictive models for protein synthesis and Glut4 translocation include common and unique
760 predictors (coregulator peptide interactions and target genes), with specific examples shown and
761 significance determined by linear regression. Each point represents the activity of a distinct ligand
762 in the cognate assay.
763 **c**) Linear regression was used to compare the predictive power of the indicated peptide interactions
764 for the indicated skeletal muscle phenotypes and target genes.
765 **d**) Linear regression was performed for ligand-dependent effects on Glut4 translocation. The
766 predictive power, r^2 of target genes and peptide interactions observed with all compounds (**1-3** and
767 **6-27**) were rank ordered, and then compared to the r^2 observed within compound series modified
768 at either C11 (**13–20**) or C3 (**6-12**) of the steroid scaffold.
769 **e**) Linear regression on the effects of the C11 substituted compounds on *Bcl2l1* expression or Glut4
770 translocation. Each point represents the effects of a separate compound.
771 See also **Methods**, **Supplementary Dataset**, and **Supplementary Figure S2.**
772
773 **Figure 3. Functional validation of the predictive target gene, Fkbp5, and GR coregulators**
774 **a–c**) Empty vector (GFP) control, and either Fkbp5 or Foxo1 expression plasmids were
775 electroporated into contralateral Tibias Anterior (TA) muscles of mice. After 7 days, the mice were
776 fasted overnight and treated with puromycin and insulin for 1 hr the TA muscles collected for

777 weighting and western blots. N= 3–4.

778 **a**) Weight of transduced TA muscles.

779 **b–c**) Western blot and quantitation of **b**) puromycin (measuring incorporation into growing
780 polypetide chains to assay insulin-mediated protein synthesis) or **c**) pAKT in transduced TA
781 muscles.

782 **d**) Effects of Dex on insulin-induced protein synthesis in C2C12 myotubes transduced with
783 lentivirus expressing the indicated shRNAs. N = 6 wells x 4 shRNAs targeting each gene.

784 **e**) Effects of Dex on insulin-induced pAKT in C2C12 myotubes transduced with lentivirus
785 expressing the indicated shRNAs. N = 6 wells x 4 shRNAs targeting each gene.

786 Data are mean + S.E.M. See also **Supplementary Figure 3.**

787

788 **Figure 4. In vitro characterization of two dissociated GR ligands with musculoskeletal**
789 **sparing activities.**

790 **a**) IL-1β-induced IL-6 production by A549 cells treated with the indicated compounds was
791 compared by AlphaLISA. N = 3.

792 **b–d**) Myotubes were assayed as described **Supplementary Figure 1** and **Methods**. N = 4-6

793 **e-f**) Mitochondrial potential of C2C12 myoblasts was compared by high content imaging. f)
794 Representative myoblasts imaged during the assay.

795 **g**) The effects of all tested compounds on IL-1β-induced secretion of IL-6 by A549 cells (y axis)
796 and primary human osteoblast mineralization (x axis). Right, Dose curves of indicated compounds
797 in the IL-6 assay.

798 **h**) Effects of the indicated C3-substituted compounds on IL-6 secretion. N = 3.

799 Data are mean + SEM. See also **Supplementary Figure 4**

800

801 **Figure 5. In vivo compound profiling and validation of on target mechanism of action**

802 **a**) Dex inhibits SR16024-dependent protein synthesis in C2C12 myotubes and right-shifts the dose

803 curve, demonstrating the SR1604 activities are on-target through GR. N = 4

804 **b**) RU-486 relieves SR11466-suppressed IL-6 secretion. IL-1β-induced IL-6 production by A549

805 cells treated with the indicated compounds was compared by AlphaLISA. N = 3

806 **c**) Plasma TNFα levels of mice treated with the indicated GR ligands (10 mg/kg Dex or SR16024,

807 or 50 mg/kg SR11466) overnight before a 1-hr LPS challenge of 1.5 mg per mouse. N = 10 mice

808 per group (5 x 2 experiments).

809 **d**) Changes in lean mass of mice in panel J were determined by whole-body NMR after an

810 additional 18-hr LPS treatment of 30 mg per mouse. N = 10 mice per group (5 x 2 experiments).

811 **e-f**) Changes in the lean mass and body weights of male C57BL/6 mice treated with (10 mg/kg

812 Dex or SR16024, or 50 mg/kg SR11466) and fasted overnight. N = 10 per group (5 x 2

813 experiments).

814 **g**) Dex and SR11466 increased the rate of glucose production, unlike SR16024. Mice were

815 subjected to a lactate-tolerance test (LTT) after overnight fast. N = 5 mice per group.

816 Data are mean+SEM. See also **Supplementary Figure 5 and Methods.**

817

818 **Figure 6. Molecular dynamics simulations reveal that C3 substitutions in the steroid scaffold**

819 **alter allosteric communication between ligand and activity.**

820 **a**) Ribbon diagram of the GR-LBD illustrates the C-terminus of helix 11 (h11) and N-terminus of

821 h3 where we observed ligand-induced conformational effects in three 1 μs simulations.

822 **b**) Distance distribution plots of the Cα distance between Met560 (h3) and Thr739 (h11).

823 **c**) Backbone Cα, C', N, and O RMSD distribution plots of the h3 and h11 regions colored magenta
824 in (**a**).
825 **d**) Dynamical network analysis of suboptimal pathways for correlated motion between E755 and
826 R614. Red arrows indicate pathways found with Dex-bound GR.
827 **e**) Histogram showing the suboptimal pathlengths with the indicated ligands.
828 **f**) Structures extracted from the Dex-bound simulations showing the R611 in (left) and out (right)
829 side chain conformations.
830 **g**) Distance distribution plots of Q570 (Cδ) and R611 (Cζ) side chain atom distances as a proxy to
831 determine the relative populations inward R611 conformations that can interact with ligand.
832
833

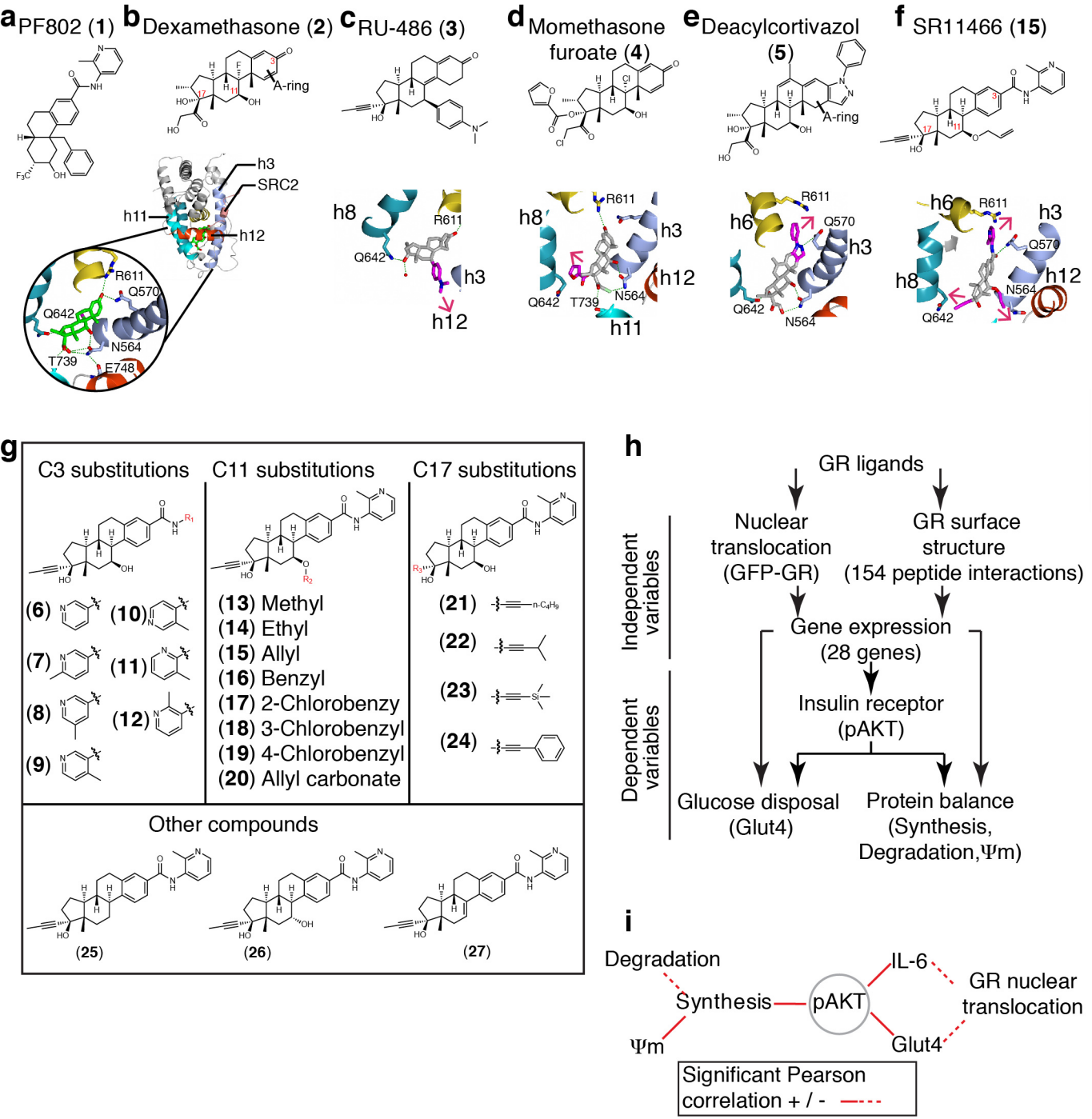
a PF802 (1)
b Dexamethasone (2)
c RU-486 (3)
d Momethasone furoate (4)
e Deacylcortivazol (5)
f SR11466 (15)
A-ring
h3
SRC2
h11
h12
R611
Q570
Q642
N564
T739
E748
h8
h6
g
C3 substitutions
C11 substitutions
C17 substitutions
(6)
(7)
(8)
(9)
(10)
(11)
(12)
(13) Methyl
(14) Ethyl
(15) Allyl
(16) Benzyl
(17) 2-Chlorobenzy
(18) 3-Chlorobenzyl
(19) 4-Chlorobenzyl
(20) Allyl carbonate
(21)
(22)
(23)
(24)
Other compounds
(25)
(26)
(27)
h
GR ligands
Nuclear translocation (GFP-GR)
GR surface structure (154 peptide interactions)
Independent variables
Gene expression (28 genes)
Insulin receptor (pAKT)
Dependent variables
Glucose disposal (Glut4)
Protein balance (Synthesis, Degradation,Ψm)
i
Degradation
IL-6
GR nuclear translocation
Synthesis
pAKT
Ψm
Glut4
Significant Pearson correlation + / -

Figure 1

a

Significant predictors	Glut4	Degradation	Ψm	Synthesis	pAKT
	#84%	46%	68%	70%	60%
	**Fkbp5*	*Ψm	*Degradation	*CHD9_1023	*Synthesis
	**Socs2*	**Socs2*	*Synthesis	*SMRT_2330	*MAPE_91
	**Bcl2l1*	Protein synthesis	CNOT1_557	**Socs2*	*SMRT_2123
	**Tsc22d3*	MAPE_91	CHD9_1023	*MAPE_91	
	*SRC1_677		SMRT_2330	**Fbxo32*	
	*SRC1_737		*Socs2*	**Sgk1*	
	Sgk1			**Irs1*	
	NRBF2_128			NCOR1_2251	
	PGC1-β_338			Ψm	
	Vav2			NELFB_328	
	SRC2_733			pAKT	
	PELP1_446			CHD9_855	

#r^2, Fraction of variance predicted by the minimal set of predictors *Minimal set of predictors

b

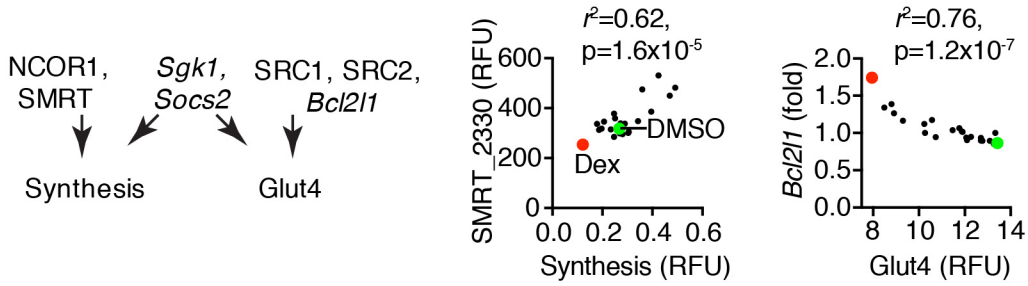

c

Peptides	Synthesis	Ψm	Degradation	pAKT	Glut4	*Bcl2l1*	*Fkbp5*	*Sgk1*	*Tcs22d3*	*Vav2*
PELP1_446	0.22	0.02	0.10	0.45	0.65	0.89	0.96	0.86	0.96	0.87
SRC1_737	0.24	0.02	0.12	0.46	0.69	0.88	0.92	0.78	0.97	0.89
SRC1_677	0.21	0.01	0.10	0.43	0.71	0.87	0.91	0.74	0.96	0.92
SRC2_733	0.26	0.02	0.13	0.50	0.73	0.85	0.90	0.72	0.97	0.92
NRBF2_128	0.18	0.00	0.10	0.38	0.65	0.83	0.89	0.70	0.93	0.89
PGC1-β_338	0.21	0.01	0.13	0.47	0.75	0.83	0.82	0.66	0.93	0.88
SMRT_2230	0.62	0.41	0.21	0.34	0.02	0.03	0.37	0.12	0.12	0.05

Coefficient of determination r^2

d

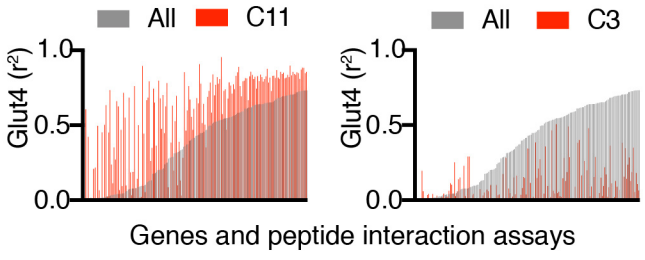

e

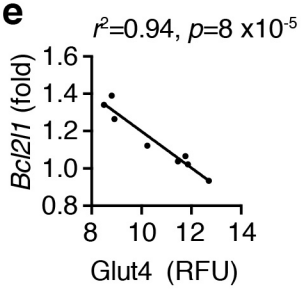

Figure 2

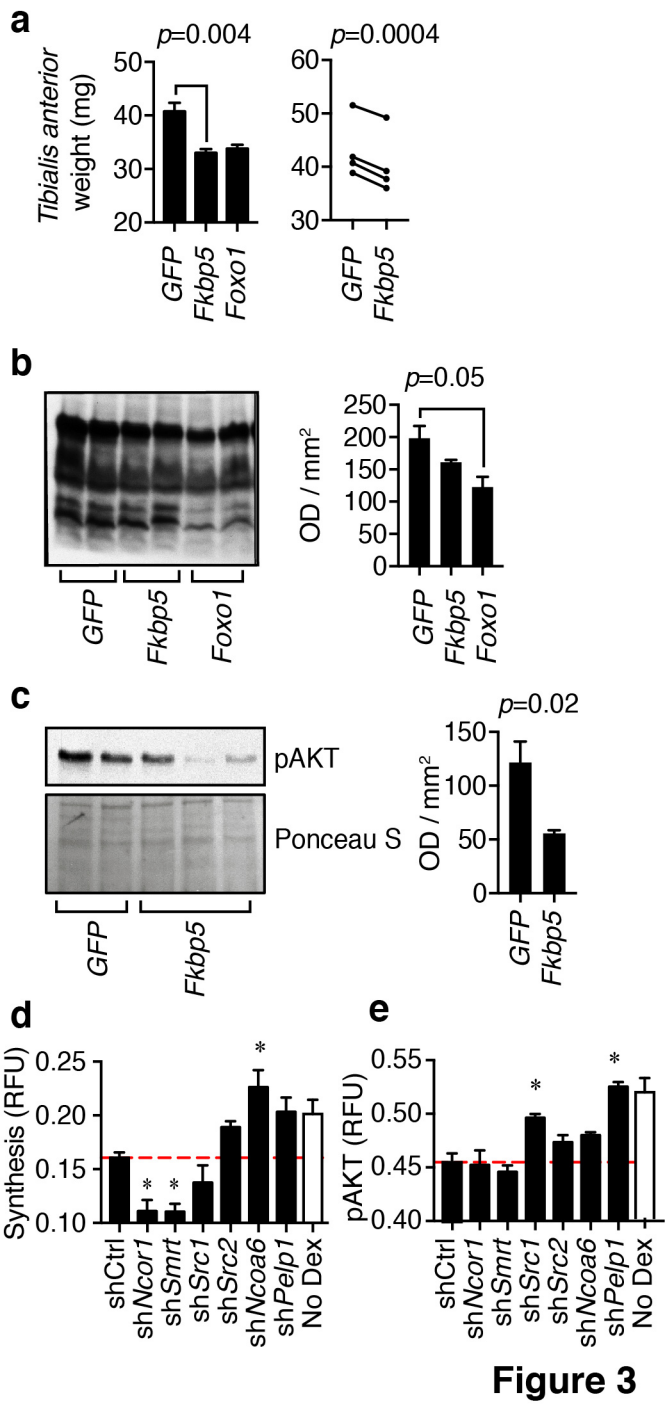
a
p=0.004
p=0.0004
Tibialis anterior weight (mg)
50
40
30
20
60
50
40
30
GFP
Fkbp5
Foxo1
GFP
Fkbp5
b
p=0.05
OD / mm2
250
200
150
100
50
0
GFP
Fkbp5
Foxo1
c
pAKT
Ponceau S
p=0.02
OD / mm2
150
100
50
0
GFP
Fkbp5
d
Synthesis (RFU)
0.25
0.20
0.15
0.10
shCtrl
shNcor1
shSmrt
shSrc1
shSrc2
shNcoa6
shPelp1
No Dex
e
pAKT (RFU)
0.55
0.50
0.45
0.40
shCtrl
shNcor1
shSmrt
shSrc1
shSrc2
shNcoa6
shPelp1
No Dex

Figure 3

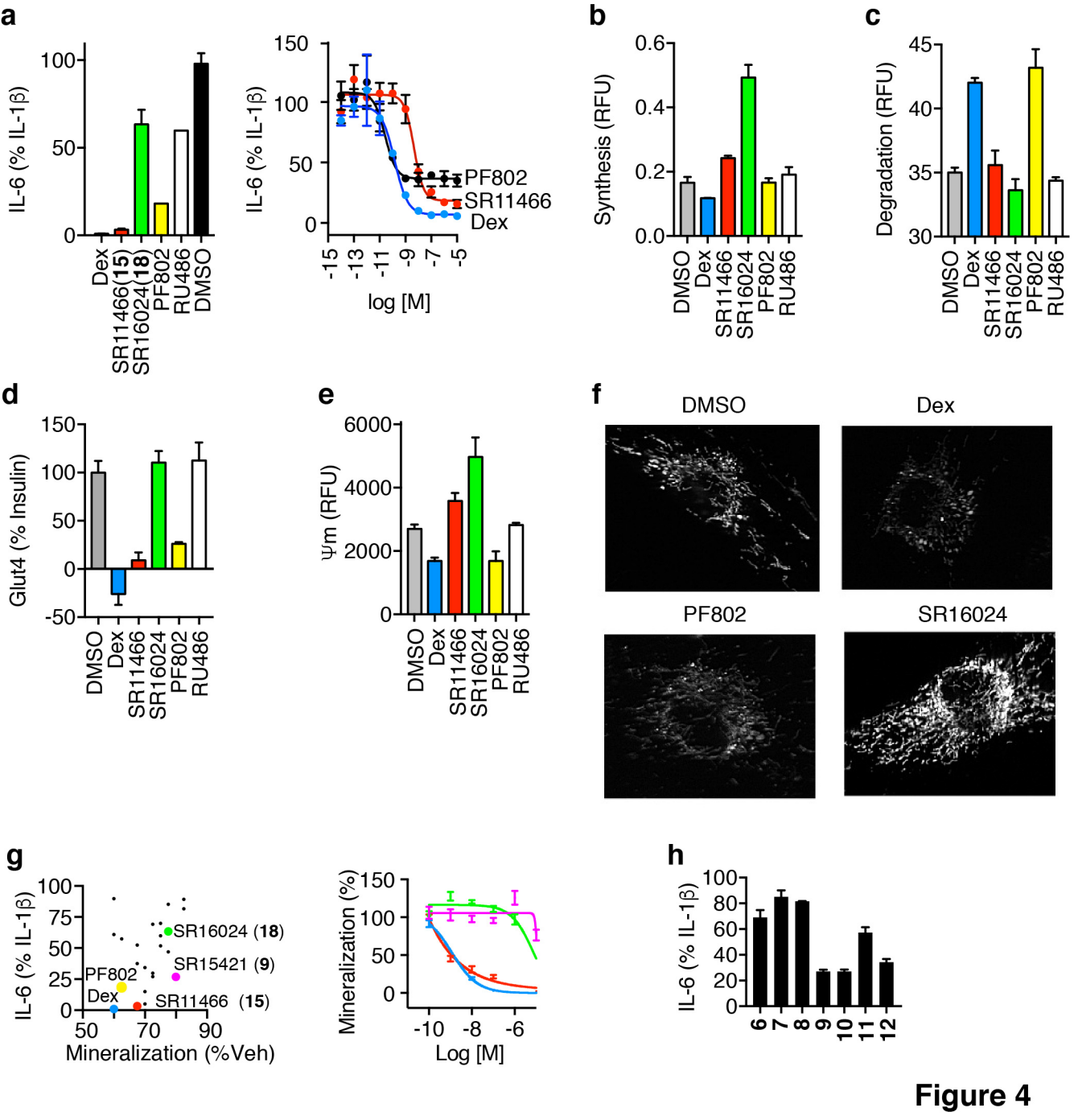
a
IL-6 (% IL-1β)
Dex
SR11466(15)
SR16024(18)
PF802
RU486
DMSO
log [M]
PF802
SR11466
Dex
b
Synthesis (RFU)
c
Degradation (RFU)
d
Glut4 (% Insulin)
e
Ψm (RFU)
f
DMSO
Dex
PF802
SR16024
g
IL-6 (% IL-1β)
Mineralization (%Veh)
SR16024 (18)
SR15421 (9)
PF802
Dex
SR11466 (15)
Mineralization (%)
Log [M]
h
IL-6 (% IL-1β)

Figure 4

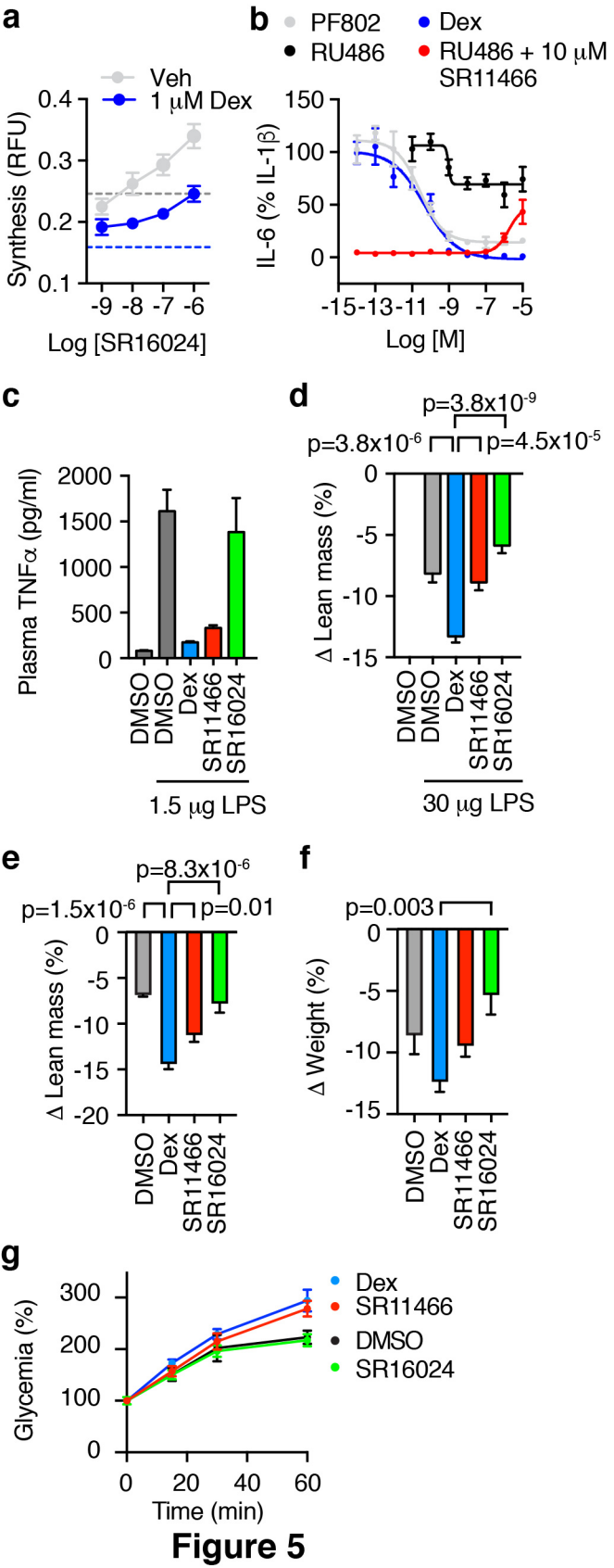
a
Veh
1 μM Dex
Synthesis (RFU)
0.4
0.3
0.2
0.1
-9 -8 -7 -6
Log [SR16024]
b
PF802
RU486
Dex
RU486 + 10 μM SR11466
IL-6 (% IL-1β)
150
100
50
0
-15 -13 -11 -9 -7 -5
Log [M]
c
Plasma TNFα (pg/ml)
2000
1500
1000
500
0
DMSO
DMSO
Dex
SR11466
SR16024
1.5 μg LPS
d
p=3.8x10-9
p=3.8x10-6
p=4.5x10-5
Δ Lean mass (%)
0
-5
-10
-15
DMSO
DMSO
Dex
SR11466
SR16024
30 μg LPS
e
p=8.3x10-6
p=1.5x10-6
p=0.01
Δ Lean mass (%)
0
-5
-10
-15
-20
DMSO
Dex
SR11466
SR16024
f
p=0.003
Δ Weight (%)
0
-5
-10
-15
DMSO
Dex
SR11466
SR16024
g
Glycemia (%)
300
200
100
0
0 20 40 60
Time (min)
Dex
SR11466
DMSO
SR16024

Figure 5

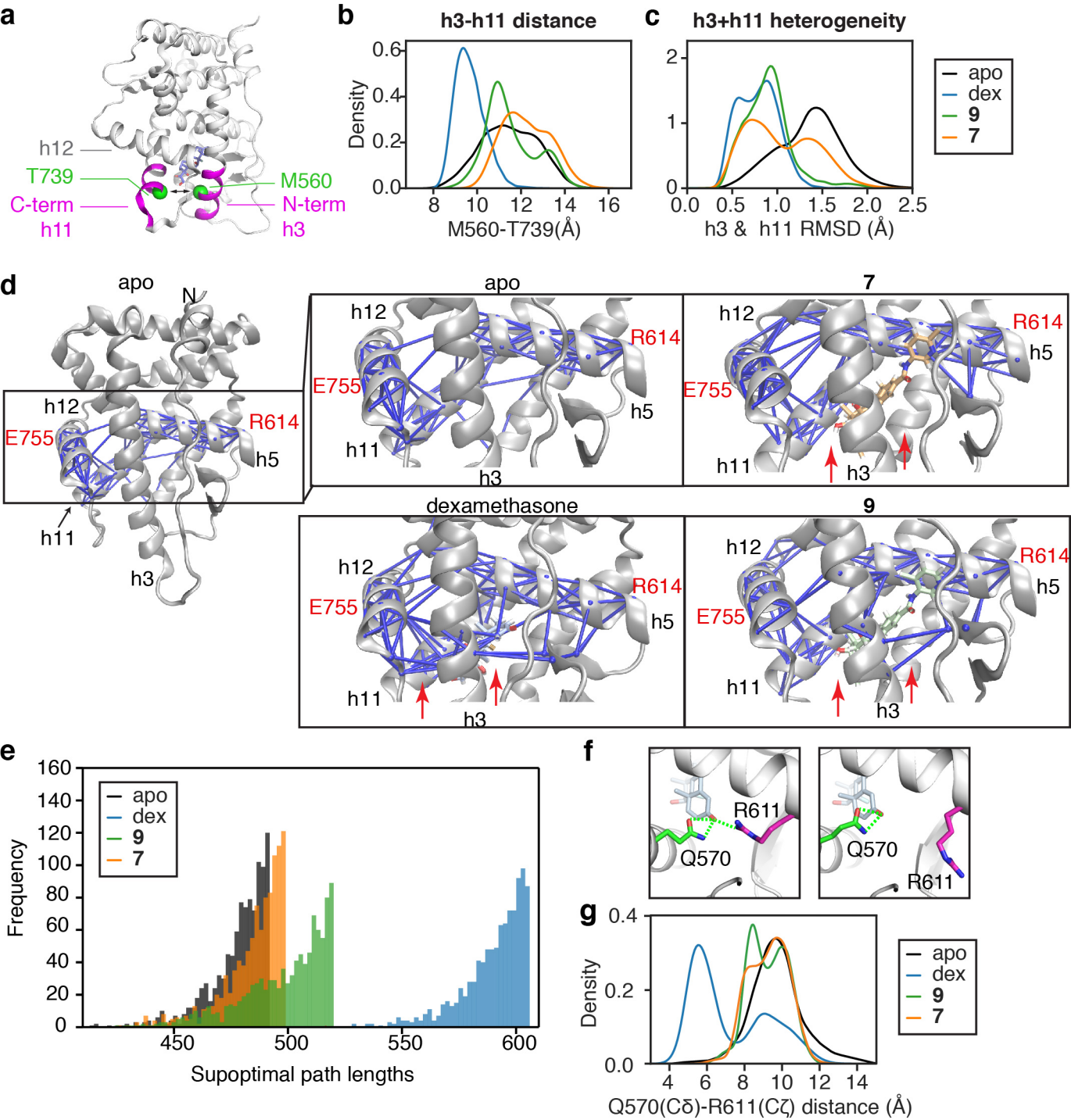
a
h12
T739
M560
C-term
N-term
h11
h3
b
h3-h11 distance
Density
M560-T739(Å)
c
h3+h11 heterogeneity
h3 & h11 RMSD (Å)
apo
dex
9
7
d
apo
N
h12
E755
R614
h5
h11
h3
7
dexamethasone
9
e
Frequency
Supoptimal path lengths
f
R611
Q570
g
Density
Q570(Cδ)-R611(Cζ) distance (Å)

Figure 6